Research Article Vol. 32, No. 5 / 26 Feb 2024 / Optics Express 8172
Optics EXPRESS

# Fiber-taper collected emission from NV centers in high-$Q/V$ diamond microdisks

TAMIKO MASUDA,[1,2] J. P. E. HADDEN,[1,3] DAVID P. LAKE,[1,4] MATTHEW MITCHELL,[1] SIGURD FLÅGAN,[1] AND PAUL E. BARCLAY[1,*]

[1]*Department of Physics and Astronomy and Institute for Quantum Science and Technology, University of Calgary, Calgary, AB, T2N 1N4, Canada*
[2]*1QB Information Technologies (1QBit), 1285 West Pender Street, Unit 200. Vancouver, BC, V6E 4B1, Canada*
[3]*Currently with the School of Engineering, Cardiff University, Cardiff, CF24 3AA, United Kingdom*
[4]*Currently with the Applied Physics Department, California Institute of Technology, Pasadena, CA 91125, USA*
[*]*pbarclay@ucalgary.ca*

**Abstract:** Fiber-coupled microdisks are a promising platform for enhancing the spontaneous emission from color centers in diamond. The measured cavity-enhanced emission from the microdisk is governed by the effective volume ($V$) of each cavity mode, the cavity quality factor ($Q$), and the coupling between the microdisk and the fiber. Here we observe room temperature photoluminescence from an ensemble of nitrogen-vacancy centers into high $Q/V$ microdisk modes, which when combined with coherent spectroscopy of the microdisk modes, allows us to elucidate the relative contributions of these factors. The broad emission spectrum acts as an internal light source facilitating mode identification over several cavity free spectral ranges. Analysis of the fiber taper collected microdisk emission reveals spectral filtering both by the cavity and the fiber taper, the latter of which we find preferentially couples to higher-order microdisk modes. Coherent mode spectroscopy is used to measure $Q \sim 1 \times 10^5$ – the highest reported values for diamond microcavities operating at visible wavelengths. With realistic optimization of the microdisk dimensions, we predict that Purcell factors of ~50 are within reach.



## 1. Introduction

Color centers in diamond are luminescent defects consisting of vacancies and substitutional impurity atoms embedded in the carbon lattice. These color centers often combine long spin coherence times [1–4] with spin-selective optical transitions [5–7]. The ability to perform all-optical spin control [8–10] and single-shot spin readout [11–13] makes these color centers promising qubit candidates for photonic quantum architectures [14–17]. In particular, the optically addressable electron spin associated with the nitrogen-vacancy (NV) center [18] has been used in successful demonstrations of quantum memories [3,19–22], spin-photon [23] and spin-spin [24–26] entanglement, and quantum teleportation [27], culminating in the demonstration of multinode quantum networks [28,29]. However, the ability to extend these proof-of-principle demonstrations to practical on- and off-chip quantum networks [30] requires the efficient generation and distribution of entanglement across remote network nodes [31]. The success rate of heralded entanglement schemes utilizing one-photon [29,32] and two-photon protocols [24,25,27] are inherently limited by the collection probability of coherent photons. For experiments using NV centers, the flux of coherent photons is limited by the small branching into the zero-phonon line of ~ 3 % and a poor collection efficiency due to total internal reflection at the diamond-air interface [33]. In turn, these shortcomings limit scalability to systems consisting of

#507325 https://doi.org/10.1364/OE.507325
Journal © 2024 Received 3 Oct 2023; revised 1 Dec 2023; accepted 2 Dec 2023; published 22 Feb 2024

Optics EXPRESS

many entangled nodes, such as quantum-repeater-based long-distance quantum communication [34] and the realization of quantum networks [30,31].

The tight confinement of light in optical resonators combining a high quality factor, $Q$, with a small mode volume, $V$, leads to enhanced light-matter interactions [35–37]. For example, by utilizing the Purcell effect [38], optical cavities have been used to enhance the photon flux from color centers in diamond [33,39–41]. While coupling between diamond color centers and optical cavities has been demonstrated using a variety of different geometries, including hybrid platforms [42–48] and tunable Fabry-Perot microcavities [33,41,49–55], realizing high $Q/V$ monolithic cavities directly from single-crystal diamond (SCD) allows for minimizing $V$ while maximizing the emitter-cavity coupling by maximizing the overlap of the emitter dipole-moment with the cavity mode. Furthermore, the use of monolithic resonators facilitates the implementation of on-chip photonic buses for efficient photon extraction [56]. This, in conjunction with the fact that the highest quality color centers are found in bulk SCD [1,57–61], has spurred the invention of fabrication techniques to further develop SCD devices [62–72].

At the visible wavelengths resonant with diamond color center optical transitions (637 nm for the NV center), SCD ring resonators produced by a thinned membrane technique have been reported with $Q \sim 3 \times 10^4$ and effective mode volume, $V_{\text{eff}} \sim 10^1\ (\lambda/n)^3$ [39]. In this wavelength range, racetrack resonators [62] fabricated using angled etching of SCD [73] have demonstrated $Q \sim 6 \times 10^4$ – the previously largest $Q$-factor reported for monolithic SCD resonators – while open Fabry-Perot microcavities have been reported with $Q{>}10^5$ [74–76]. However, the increased length of these resonators limits the smallest achievable $V$. Photonic crystal nanocavities, on the other hand, have been demonstrated with $Q \sim 1 \times 10^4$ [67], and ultra-low $V_{\text{eff}}{<}(\lambda/n)^3$ [70,77]. Recently, quasi-isotropic undercut etching [78] has been used to create high $Q/V$ microdisks [69,79,80] and photonic crystal cavities [81,82]. While the latter have been realized at visible wavelengths, and coupling to color centers have been demonstrated [83,84], previous studies of diamond microdisks have been predominantly limited to telecommunication wavelengths and applications related to cavity optomechanics [80,85–88]. Thus, there is an unexplored potential for monolithic diamond microdisks to provide state-of-the-art Purcell enhancement of NV emission that can be efficiently collected through waveguides.

As a first step of exploration, we demonstrate coupling between an ensemble of NV centers and whispering gallery modes (WGM) in SCD microdisks by evanescently probing the microdisks modes with a fiber-taper waveguide. Operating at room temperature, the NV centers photoluminescence (PL) provides a spectroscopic tool by acting as an internal, broadband light source. The NV center PL preferentially couples to the WGMs of the cavity, thus enabling broadband PL mode spectroscopy over cavity free spectral ranges (FSR). Using this tool, alongside high resolution coherent mode spectroscopy, which reveals $Q$-factors as large as $\sim 10^5$, we observe complex cavity spectra that suggest further diamond microdisk development is needed before witnessing a significant lifetime reduction due to the Purcell effect. To inform the direction of the development of next generation diamond microdisks, we analyze the coupling of the NV centers to the microdisk and the coupling between the microdisk and the fiber taper.

The remainder of this paper is organized as follows. We begin by detailing the fiber-taper microdisk system, followed by an outline of the experimental procedure. Next, we study the fiber-taper collected PL spectra by comparing the measured intensities to those expected from a simple model of the system, based on the $Q$-factors extracted from the fiber-taper transmission measurements. Following this, we use broadband FSR data to perform mode-family identification to gain further insight into the fiber-taper microdisk system. Finally, in the outlook, we discuss optimization of the microdisk geometry with regards to Purcell enhancement of spontaneous emission from color centers embedded in the microdisks.

Optics EXPRESS

## 2. Experimental setup: fiber and free-space coupling

In the experiment presented in this work, we study SCD microdisks fabricated following the quasi-isotropic undercut etching process reported in Refs. [69,79,80]. The starting material was diamond chips with a ⟨100⟩ crystal orientation grown using chemical vapor deposition (Element Six). These chips are "optical grade", with an estimated nitrogen impurity concentration of <1 ppm. In brief, the microdisk fabrication procedure involves three main steps: (1) writing device patterns using electron beam lithography (EBL); (2) transferring patterns to a silicon nitride hard mask and subsequently to the diamond via anisotropic reactive ion etching; and (3) undercutting of the devices with a quasi-isotropic etch [78,79]. As shown in Fig. 1(a), the resulting microdisks are supported by thin pedestals and have radius $r \sim 2-4\,\mu$m and thickness $t \sim 0.8-1.0\,\mu$m.

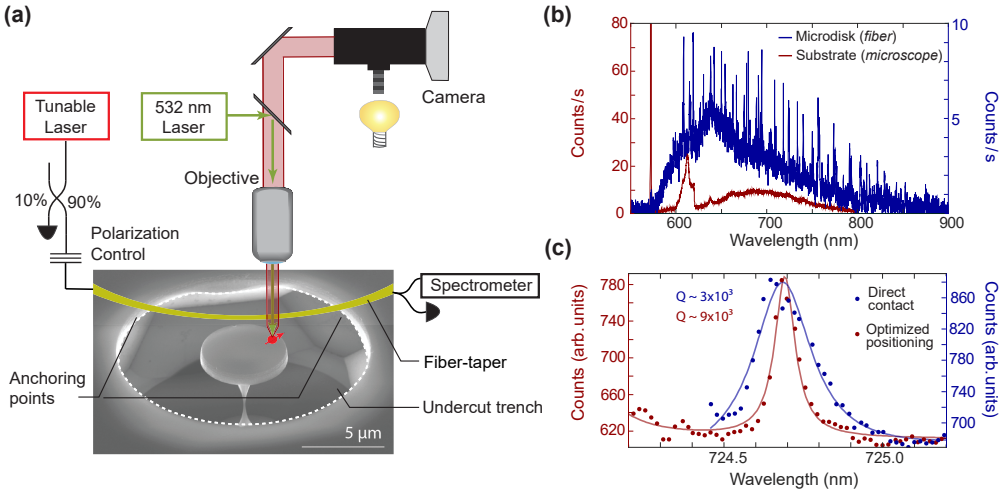


**Fig. 1.** **(a)** A simplified schematic of the experimental setup used for fiber-taper collected NV center PL and cavity transmission measurements. Included is an SEM image of one of the diamond microdisks studied in this work. Note that the scale bar applies to the SEM image only – the dimpled fiber-taper is not drawn to scale. The white dashed line indicates the edge of the trench defined by the microdisk etching. The points of contact, where we anchor the fiber taper to keep the distance between the fiber taper and the microdisk constant, are labeled as anchoring points. The objective lens used for free-space excitation can be manually moved using an *xyz* translation stage. **(b)** In blue: fiber-collected PL from a diamond microdisk of $[r, t]$~[2.5 µm, 850 nm]. In burgundy: reference spectrum showing the NV center PSB obtained via confocal microscope collection of NV center PL signal from an implanted electronic grade diamond substrate, taken with an alternative setup. **(c)** fiber-taper collected PL spectroscopy for two fiber positions. Positioning the fiber carefully next to the device yield $Q \sim 9 \times 10^3$ (burgundy). When the fiber is touching the device (blue line), a threefold reduction of the $Q$-factor is observed, resulting in $Q \sim 3 \times 10^3$.

The experimental setup used to study both the fiber transmission and PL from the microdisks is shown schematically in Fig. 1(a). The fiber taper is positioned within the near-field of the microdisks using stepper-motor translation stages (Suruga Seiki), while imaged with white light on a CCD camera. When coupling the fiber taper to the microdisk, it is important to avoid interactions with the unpatterned substrate surrounding the ring-shaped windows defining the microdisks. Therefore, the fiber taper is produced with a *dimple* [89]. The fabrication procedure of the dimpled fiber taper goes as follows. First, a single-mode optical fiber (Nufern 630-HP) designed for operation at visible wavelengths is heated using a stationary (no dither) hydrogen

Optics EXPRESS

torch setup and stretched to produce a fiber taper that is single mode at $\sim 640$ nm. Ideally, this corresponds to a fiber-taper radius of $a \sim 230$ nm [90]. The dimple is then created by annealing the taper while it is wrapped around a ceramic knife edge. The dimpled fiber-taper is mounted in a U-bend shape, which provides mechanical stability and resilience.

To measure the transmission through the fiber taper, we sweep the output of a narrow linewidth tunable diode laser, while monitoring the transmitted signal on a photodiode. To maximize the contrast of the observed cavity resonances, the polarization of the incoupled light is adjusted using a fiber paddle controller. Wavelength- and time-dependent fluctuations in the laser output can make it difficult to discern low-contrast features in the transmission measurement. To mitigate this effect, we used the most stable laser available to us in the PSB wavelength range (Newport Velocity, $\lambda = 735 - 740$ nm, $\delta\nu \leq 200$ kHz) and applied a tap-off of the laser output to remove the laser-related features from the transmitted signal, thus aiding the identification of microdisk resonances.

For the fiber-taper collected PL measurements, an ensemble of NV centers intrinsic to the optical grade diamond are excited from the top using a 532 nm laser with power on the order of mW using a microscope objective of numerical aperture (NA = 0.55) producing a diffraction limited focal spot ($\sim 680$ nm diameter). The resulting PL from the NV center PSB provides an internal cavity light-source that can be used to characterize the optical modes of the microdisk [91]. The microdisk-filtered PL is collected by the fiber taper and detected by a spectrometer. An example spectrum collected using this system is shown by the blue curve in Fig. 1(b). Sharp features associated with coupling to individual microdisk modes are evident over a broad range extending from $600 - 800$ nm. This broad signal extends over the same wavelength range as the reference spectrum (burgundy) of the NV center PSB [92,93]. The reference spectrum was measured through direct free-space confocal microscope collection of PL from implanted NV centers in an electronic grade sample, using an alternative setup. It represents the standard shape of a PL spectrum from a diamond sample excited by 532 nm light, including NV emission and Raman signatures at 572 nm and $\sim 612$ nm [91]. The shape of the fiber-taper collected signal is dependent on factors including the position of the excitation laser and the fiber taper, respectively. We therefore note that the reference spectrum should not be used to compare collection efficiencies, as any variation between the two spectra arises due to the different collection methods.

At the close proximity required for evanescent coupling, the fiber taper is attracted to the microdisk, often resulting in unwanted contact between the fiber taper and the disk [62]. However, it is possible to completely mitigate this contact by taking advantage of the geometry of the ring shaped trench in the substrate surrounding the microdisk that is defined during the undercut etching step (see Fig. 1(a)). While maintaining sufficient separation between the sample surface and fiber taper to prevent attraction, the taper can be roughly positioned at the desired lateral location. Then, by lowering the fiber quickly, contact between the outer edge of the trench and the fiber taper prevents the fiber from touching the microdisk. Furthermore, anchoring the taper at the edge of the trench prevents the fiber from moving, thus maintaining a constant separation between the fiber taper and the microdisk. The importance of careful positioning of the fiber taper is illustrated in Fig. 1(c), where PL measurements were recorded for two different fiber taper positions. An increase in the cavity linewidth, and corresponding reduction in $Q$-factor, is observed when the fiber is in contact with the microdisk (blue line in Fig. 1(c)). Intuitively, this reduction in $Q$-factor can be explained by the fact that, upon contact, the fiber effectively becomes part of the cavity and induces parasitic loss [94] such as scattering of light out of the cavity and into radiation modes.

Optics EXPRESS

## 3. Fiber-coupled NV center photoluminescence and coherent mode spectroscopy

In this section, we explore the use of fiber-taper collected PL from the NV centers as a means to characterize the microdisk optical mode spectrum over the broad PSB wavelength range. In an ideal case, NV center PL collected by the fiber taper and imaged on the spectrometer would reveal the bare microdisk cavity mode spectrum, where the relative peak intensities are governed by the $Q/V$ ratio of the individual modes. However, in practice, this is not the case as fiber-taper collected PL is affected by the coupling between the fiber taper and the microdisk – an effect that we elucidate in the analysis presented below.

Figure 2 shows fiber-taper collected PL and fiber-taper transmission measurements for two microdisks, labeled $A$ and $B$ with dimensions $[r, t]$~$[2.0\,\mu\text{m},\ 800\,\text{nm}]$ and $[r, t]$~$[3.10\,\mu\text{m},\ 850\,\text{nm}]$, respectively. The correlation between peaks in PL and dips in the transmission spectrum, confirms that the observed PL peaks are signatures of microdisk optical modes. However, the strongest fiber-collected PL signals do not, in general, correspond to the highest-$Q$ microdisk modes measured in transmission. Rather, the peaks in PL can be aligned with lower-$Q$ microdisk modes coupled more strongly to the fiber taper. Below we analyze both transmission and PL data to determine the relative impact of the optical mode $Q$-factor and coupling parameters on the observed signals.

The fiber-taper collected PL intensity, $I_j$, of microdisk mode $j$, can be predicted by modeling the fiber-taper–microdisk collection system using an input-output formalism. Mode $j$ is defined to have field amplitude $a_j$, total loss rate $\kappa_j$, and resonant frequency $\omega_j$ [94]. The mode is excited at frequency $\omega$ by a source term $s_j$, whose strength depends on the emission of the NV PSB into mode $j$. Given external coupling rate $\kappa_j^e$ from the microdisk mode into the forward propagating (i.e. measured) mode of the fiber taper, the collected PL intensity from mode $j$ is $I_j = |\sqrt{\kappa_j^e} a_j|^2$. The cavity mode equation of motion is [95]:

$$\frac{da_j}{dt} = \left(i\Delta\omega_j - \frac{\kappa_j}{2}\right) a_j + s_j\ , \tag{1}$$

where $\Delta\omega_j = \omega - \omega_j$. This can be solved for a steady-state value of $a_j$ to obtain:

$$I_j = \frac{\kappa_j^e |s_j|^2}{(\Delta\omega_j)^2 + (\kappa_j/2)^2}\ . \tag{2}$$

Note that similar expressions can be derived for the symmetric and anti-symmetric modes of doublet resonances observed for the highest $Q$ modes of our microdisks [96].

Equation (2) can be expressed in terms of $Q_j = \omega_j/\kappa_j$ and $Q_j^e = \omega_j/\kappa_j^e$ and evaluated on resonance to obtain a peak height of:

$$I_j(\Delta\omega_j = 0) = 4Q_j \frac{Q_j}{Q_j^e} \frac{|s_j|^2}{\omega_j}\ . \tag{3}$$

From this expression, the emission into the fiber taper for mode $j$ can be enhanced by increasing $Q_j$ or by increasing the coupling strength to the fiber taper, as determined by $Q_j/Q_j^e$. The ratio of $Q_j$ to $Q_j^e$ is responsible for the dramatic differences in peak heights observed in Fig. 2, which we will quantify further below.

Microdisk $A$ supports a high $Q \sim 80\,000$ mode alongside lower $Q$ modes, as shown in the laser transmission measurements in Fig. 2(a) and Fig. 2(b). Microdisk $B$, on the other hand, has a more complicated mode spectrum, as shown in Fig. 2(c) and 2(d). In Fig. 2(b), we see that mode $R_1$ of microdisk $A$ has $Q$-factor approximately 4 times larger than that of mode $R_2$. However, the PL associated with $R_1$ is barely discernible, while $R_2$ exhibits a strong peak. On the other hand, Fig. 2(d) shows that for microdisk $B$, the higher-$Q$ mode $R_1$ does have a larger peak

Optics EXPRESS

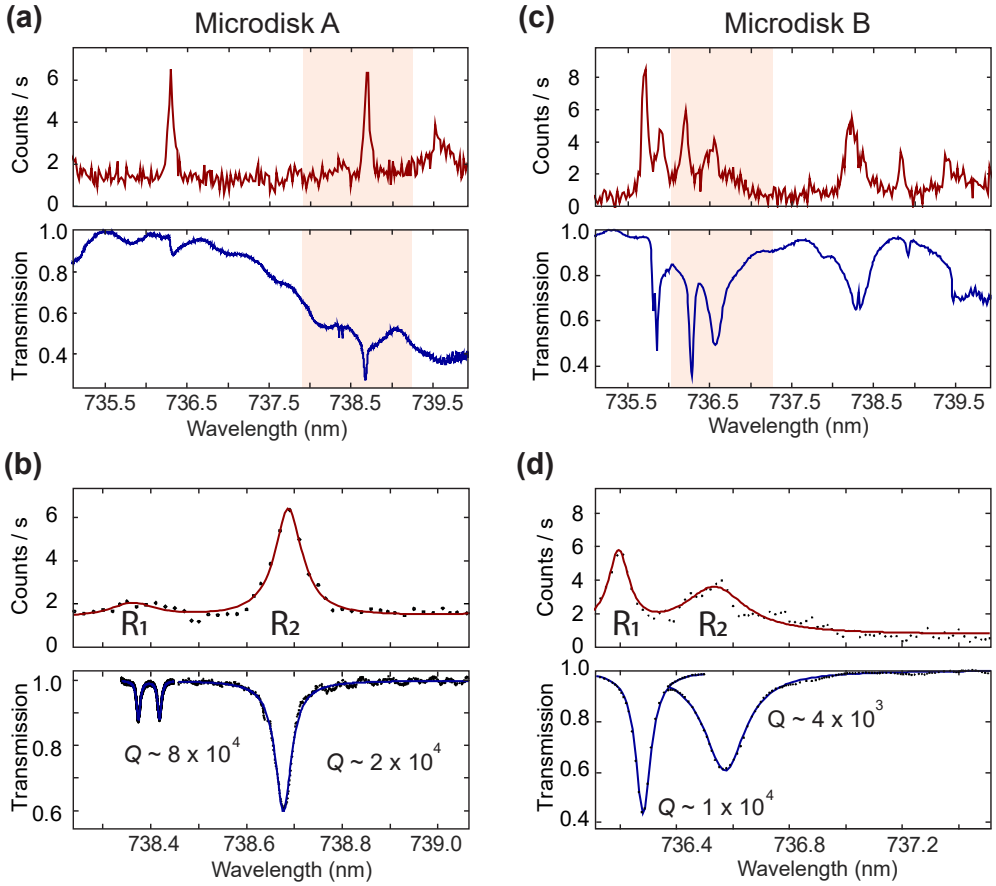


**Fig. 2.** Transmission (blue) and photoluminescence (burgundy) measurements for microdisk $A$ (a, b) with $[r, t]$~[2.0 μm, 800 nm] and microdisk $B$ (c, d) with $[r, t]$~[3.1μm, 850 nm]. Panel (a) and (c) show the measurement over a broad wavelength range. The shaded regions are expanded to produce the fits displayed in panel (b) and (d). Note that the transmission spectra in (a) and (c) were normalized to the transmission of the fiber taper when it was positioned far from the microdisk, whereas the transmission spectra in (b) and (d) were normalized to a fit of the wavelength dependent background centered around the resonance. For the transmission measurements in (c) and (d), the fit for each resonance has been performed independently, taking into consideration the modulated background, and superimposed in the figure. Discrepancies in PL and transmission data regarding resonance center wavelength are attributed to slight calibration errors (<0.1 nm).

Optics EXPRESS

height in PL compared to the lower-$Q$ $R_2$ mode. The data illustrates that the peak height is not always an accurate measure of the $Q$-factor, and that variations in the peak height can be strongly influenced by differences in $Q_j^e$ and $s_j$.

To quantify further the impact of the different contributions to the peak height, we define the *peak height ratio*, $\alpha$, for a given pair of modes:

$$\alpha = \frac{I_{R_1}(\omega_{R_1})}{I_{R_2}(\omega_{R_2})}. \tag{4}$$

Table 1 compares three distinct versions of $\alpha$, calculated under different assumptions to reveal the effect of $Q_j$ and $Q_j^e$ on the relative peak height. Here, $\alpha_I$ is the ratio of the measured PL intensity values. We next use Eq. (3) to calculate $\alpha$ for two different scenarios using the values of $Q_j$ extracted from the laser transmission measurement in Fig. 2(b) and Fig. 2(d). In the following, we make the assumption that $s_{R_1} = s_{R_2}$, a reasonable assumption on the grounds that the measurements are performed at room temperature where the microdisk–NV center system is in the "bad emitter regime". In this regime, as long as modes $R_1$ and $R_2$ have comparable mode volume – an assumption we will revisit below – emitters behave as a white light source [51,97,98], and thus $|s_j|^2$ is expected to be proportional to the intensity of the PSB at $\omega_j$, approximated to be constant over the narrow wavelength ranges studied in Fig. 2(b) and Fig. 2(d). In this regime, we do not expect to observe any lifetime reduction. Nevertheless, due to the Purcell effect, PL from the NV centers is preferentially emitted into the WGMs of the microdisk. We therefore start by assuming equal fiber-taper coupling for both modes, i.e. $Q^e_{R_1} = Q^e_{R_2}$, and calculate the expected Purcell enhanced peak intensity and the associated $\alpha_P = (Q_{R_1}/Q_{R_2})^2 \omega_{R_2}/\omega_{R_1}$. We next investigate the effect of different fiber-taper coupling to each mode. To this end, we extract $Q_j^e$ from the resonance contrast and the linewidth of each resonance, allowing us to calculate the corresponding $\alpha_F = \alpha_P(Q^e_{R_2}/Q^e_{R_1})$. We followed Refs. [94,99] to extract $Q_j^e = Q_j(K+1)/K$ from the fits in Fig. 2(c) and (d), where $K = (1-T^2)/(1+T^2)$ is the coupling coefficient given by the ratio of the fiber-cavity coupling rate and the sum of all other loss rates of the cavity, and $T$ is the measured on-resonance fiber-taper transmission. We summarize our findings in Table 1.

**Table 1. Peak height intensity ratios $\alpha$ and related $Q$-factors for the modes in Fig. 2. Here, $\alpha_I$ is the measured peak height ratio, whereas $\alpha_P$ and $\alpha_F$ are calculated using Eq. (3) where $\alpha_P$ assumes identical $Q_j^e$ whereas $\alpha_F$ uses $Q_j^e$ extracted from the fits.**

| Microdisk | $Q_{R_1}$ | $Q_{R_2}$ | $Q^e_{R_1}$ | $Q^e_{R_2}$ | $\alpha_P$ | $\alpha_F$ | $\alpha_I$ |
|---|---|---|---|---|---|---|---|
| *A* | $8\times10^4$ | $2\times10^4$ | $2.5\times10^6$ | $1.6\times10^5$ | 16 | 1.0 | 0.32 |
| *B* | $1\times10^4$ | $4\times10^3$ | $6.8\times10^4$ | $3.7\times10^4$ | 6.3 | 3.4 | 1.6 |

For microdisk $A$, the cavity transmission spectrum, used to calculate $\alpha_P$, predicts $I_{R_1}$ to be 16 times larger compared to $I_{R_2}$. However, after considering the fiber-taper coupling strength, we predict that $I_{R_1}$ should be of similar magnitude (1.0) as $I_{R_2}$, as quantified by $\alpha_F$. This demonstrates how the microdisk-fiber-taper coupling strength, quantified by the ratio $Q_j/Q_j^e$, can compensate for a lower $Q_j$ when determining PL peak height [94]. Furthermore, the order of magnitude reduction from $\alpha_F$ to $\alpha_I$ points towards other factors affecting the system. For comparison, a similar, but less drastic tendency, is observed for Microdisk $B$.

We next elucidate on possible explanations accounting for the observed variations in $\alpha_I$. For microdisk $A$, the discrepancy between $\alpha_F$ and $\alpha_I$ can be attributed to limited spectrometer resolution – the peak in PL is not fully captured by the spectrometer owing to the high $Q$-factor and doublet nature of mode $R_1$. Note that by sending the resonant laser straight to the spectrometer, we estimate the spectrometer resolution to be $\delta\lambda \simeq 15$ pm, corresponding to a spectrometer limited $Q_S = 5\times10^4$ – cavity resonances with $Q$-factors exceeding $Q_S$ can not be reliably resolved [43]. Furthermore, a non-unity $|s_{R_1}/s_{R_2}|$ would be manifested by variations in $\alpha_I$. However,

Optics EXPRESS

the present data is insufficient to conclude whether or not our assumptions for $s_j$ are valid. In particular, rather than approximating the PSB to be a white light source, one could model the NV center emission rate into each mode, as demonstrated for a single NV center coupled to a Fabry-Perot cavity [49]. A closer agreement between $\alpha_F$ and $\alpha_I$ is found for Microdisk *B*. However, a disagreement is still present – a factor of $\sim 2$ difference between $\alpha_F$ and $\alpha_I$. This could be explained by differences in the mode volume, as will be discussed further below. Also note that differences in spatial overlap of the microscope spot used to excite NV centers within each microdisk mode could lead to discrepancies in the measured peaks heights, however, for the objective used here this effect was not noted to strongly affect the measured spectra.

## 4. Microdisk mode identification and impact on the fiber-coupled NV center emission

To better understand the coupling between the fiber taper and the microdisks, we next identify microdisk WGM families using individual PL resonances. We start by identifying the cavity mode families based on the free spectral range. Next, we elucidate how modes of different order couple to the guided mode in the fiber taper.

Note that in this study we tested microdisks with varying radius ($r \sim 2-4\,\mu$m) and thickness ($t \sim 800-1000\,$nm). In our devices, microdisk thickness is not well controlled and varies with radius due to the nature of the diamond undercut process. This results in significant uncertainty in $t$, which can complicate the comparison of measured and theoretical mode spectra. To alleviate these complications, in this section we focus on microdisk *C* ($[r, t]$=[2.6 μm, 850 nm]), owing to its clean fiber-coupled PL spectrum that consists of strong peaks occurring at consistently spaced intervals (Fig. 3(a)). These peaks can be more easily grouped in a single mode family than modes from the more complicated spectra obtained for microdisk *A* and *B*.

### 4.1. Modal free spectral range

Microdisk mode families are classified by TE (TM)$_{p,q}$, for predominantly transverse electric (magnetic) polarization and WGM radial (vertical) order number $p$ ($q$). For a given polarization and $(p, q)$, there exists a discrete spectrum of modes with a range of allowed azimuthal order number $m$. The FSR, defined as the spacing between mode $m$ and mode $m+1$ of the same family, can be estimated according to:

$$\mathrm{FSR}(m) = 2\pi R n_{\mathrm{eff}}\left(\frac{1}{m} - \frac{1}{m+1}\right), \tag{5}$$

where $n_{\mathrm{eff}}$ is the effective refractive index, dependent on the mode family and varying slowly with $m$. Modes of different families can be distinguished by measuring FSR($\lambda_j$) of regularly spaced resonances of wavelengths $\lambda_j$ and determining $n_{\mathrm{eff}}$. Comparison with simulated values of FSR can then be used to determine the polarization and $(p, q)$ of each mode family.

Figure 3(a) shows the cavity mode spectrum for microdisk *C*. In the following analysis, we focus on the prominent resonances, which we predict are from the same mode family. Although lower intensity peaks are present in the spectrum, which indicates the presence of additional microdisk modes, trying to assign further mode families would be speculative; we therefore limit our analysis to the most prominent modes. The measured FSR for the dominant resonances in the spectrum are plotted in Fig. 3(b), along with the FDTD simulated FSR values for several different mode families. These simulations were obtained using the MEEP open-source software package [100]. The measured FSR values are significantly larger compared to the simulated FSR values of the fundamental $\mathrm{TE}_{00}$ and $\mathrm{TM}_{00}$ modes. Accounting for an uncertainty in the radius on the order of $\sim 10\,$nm (EBL resolution) and an uncertainty in the thickness $\sim 100\,$nm (defined during the etching process and estimated via SEM), does not explain this difference.

Optics EXPRESS

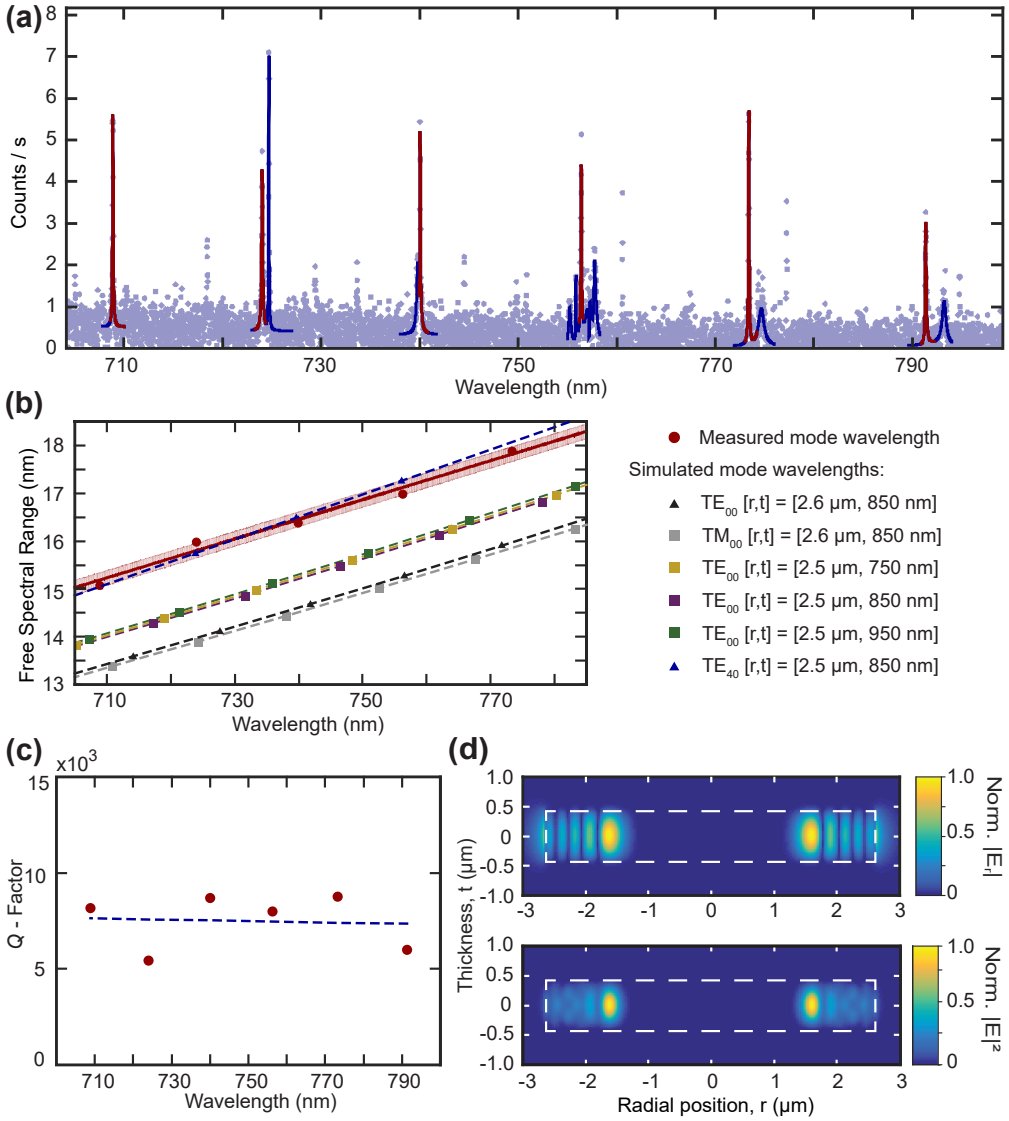


**Fig. 3.** **(a)** PL from microdisk $C$ with dimensions $[r, t]$=[2.6 µm, 850 nm]. The blue lines show multiple Lorentzians fitted to the cavity modes. The burgundy lines are hand-selected resonances belonging to the same mode family, based upon the FSR. **(b)** Comparison between measured and simulated FSR($\lambda_m$). The burgundy line shows a linear fit to the measured FSR from (a). The shaded area accounts for the uncertainty in the fit, calculated from the standard deviation of the residuals. **(c)** $Q$-factor for the burgundy resonances in (a) as a function of wavelength. **(d)** Simulated electric field profile for the $TE_{40}$ mode. Top panel: electric field in the radial direction, $E_r$. Bottom panel: total electric field squared, $|E|^2$. The white box indicates the physical extent of the microdisk.

Optics EXPRESS

This is illustrated by the simulated values in Fig. 3(b) accounting for a range of geometries. The high-intensity resonances in Fig. 3(a), therefore, do not appear to be fundamental modes.

As alluded to by the typically dense mode spectra, simulations confirm that for the dimensions of these microdisks high-$Q$ modes of both higher radial and vertical order exist. As the radial order increases, $n_{\text{eff}}$ decreases and FSR as a function of wavelength increases. Consistent with these trends, the FSR of the $TE_{40}$ mode is found to be of similar magnitude to the measured values (Fig. 3(b)). Note that, the $TE_{40}$ family has simulated radiation limited $Q>10^5$ over the entire measured range – a trend consistent with the measured $Q$-factors in Fig. 3(c), where the average $Q_{\text{avg}} = 7.4 \times 10^3$ shows no clear wavelength dependence, thus indicating that the measured modes are not radiation limited [101,102]. In Fig. 3(d), we plot simulated profiles of the $TE_{40}$ mode's dominant radial field component and its field intensity. As described below, this mode phase matches well with the fiber taper. This effect is primarily responsible for the mode's strong coupling to the waveguide, and overcomes the coupling penalty that arises from the strong confinement of the mode within the microdisk due to its higher order nature [103]. Note that coupling between longitudinal components of the microdisk and fiber-taper mode are small but non-zero, and may be of interest in some applications, for example those involving chiral photonic effects [104]. The larger mode volume associated with higher-order $TE_{40}$ modes is consistent with the difference in the observed $\alpha_{\text{I}}$ ratios – as shown below, the $TE_{40}$ mode have $V \sim 3$ times larger compared to the fundamental TE $(TM)_{00}$ modes.

### 4.2. Fiber coupling

The preferential fiber-taper coupling to the higher-order modes compared to the fundamental modes can be explained by their relative differences in phase matching to the fiber taper. For fiber-taper position defined by radial, $\rho$, and azimuthal, $\phi$, coordinates with respect to the microdisk center, a taper with propagation wavenumber $\beta_f$ along the taper axis has electric field varying as $\exp(-i\beta_f \rho \sin\phi)$ [103]. For a microdisk with a mode field varying as $\exp(im\phi)$, the phase-matching requirement is $m_{\text{pm}} \sim \beta_f \rho$ [103].

To evaluate whether phase matching describes the strong coupling to the $TE_{40}$ mode, we calculate its azimuthal mode number $m$ and the wavenumber of the fiber-taper waveguide, from which we find good agreement between $m$ and $m_{\text{pm}}$. Assuming the fiber taper has the waist radius expected for a single-mode fiber at 640 nm [90], and evaluating the approximate $\beta_f$ for the wavelengths studied here at ~ 740 nm, an $m_{\text{pm}}$ of ~27 is required for ideal phase-matching [90]. Table 2 demonstrates that, while the fundamental modes show nearly twice the desired angular momentum, the higher-order mode identified through FSR matching has $m$ close to $m_{\text{pm}}$ and therefore, favourable phase matching could explain the preferential coupling. While it is not uncommon to couple to microdisk modes demonstrating $m \sim 2 \times m_{\text{pm}}$ [103], in such instances the devices are often made extremely thin to relax the phase-matching requirements by boosting the intensity of the microdisk field that interacts with the fiber taper. Table 3 shows that the normalized microdisk thickness, $\tilde{t} = t/\lambda$, of the microdisks studied here are over twice the value of other demonstrated microdisk devices. This is consistent with the stringent phase-matching requirements limiting the coupling to lower-order modes in our system. Finally, Table 2 shows the difference in $V_{\text{eff}}$, defined by the peak field intensity $|E_{\text{max}}|$, expected for the fundamental and $TE_{40}$ modes. Here we assume that the fundamental modes are standing waves while the $TE_{40}$ mode is a traveling wave, as observed in measurements of $R_1$ (likely fundamental) and $R_2$ ($TE_{40}$), which are found to be a doublet and a singlet resonance, respectively. The variations in $V$ for mode $j$, and the consequential change in $s_j$, combined with the aforementioned differences in phase matching between the different microdisk modes and the fiber taper is reflected by the observed discrepancy in $\alpha_{\text{I}}$ (see Table 1).

Note that as the microdisk thickness decreases, phase matching to the lower order modes will improve. However, for the range of thicknesses studied here, this effect is not expected

Optics EXPRESS

**Table 2. Comparison of fundamental TE (TM)$_{00}$ and TE$_{40}$ modes of radial order $m$ for select resonances near 740 nm, relative to the phase-matched $m_{ideal}$ required for optimal fiber-taper coupling. The mode volume $V_{eff}$ is calculated by assuming the fundamental modes to be standing waves, and the TE$_{40}$ to be a traveling wave.**

| Mode | $\lambda_0$ (nm) | $m_{pm}/m$ | $V_{eff}\,(\frac{\lambda_0}{n})^3$ |
|---|---|---|---|
| TM$_{00}$ | 738 | 0.58 | 29 |
| TE$_{00}$ | 742 | 0.59 | 33 |
| TE$_{40}$ | 741 | 0.91 | 84 |

**Table 3. Comparison of device thickness normalized to the wavelength of study for several experimentally demonstrated microdisk geometries.**

| Material | $\lambda_0$ (nm) | $t$ (nm) | $\tilde{t}\left(\frac{\lambda_0}{n}\right)$ |
|---|---|---|---|
| Silicon [101] | 1550 | 344 | 0.8 |
| GaP [43] | 700 | 250 | 1.2 |
| Diamond [80] | 1550 | 940 | 1.4 |
| Diamond (this paper) | 735 | 850 | 2.8 |

to affect the dominant fiber-collected mode. A similar effect occurs as the microdisk radius changes. For the larger variation in radii considered here, this effect will be significant and may change the family of the dominant modes observed in the PL spectrum of the small (2.0 $\mu$m) microdisks compared to those of the large (3.5 $\mu$m) microdisks. As discussed above, accurately identifying modes becomes more challenging as device dimensions increase, and this process was not attempted for microdisks beyond microdisk C.

## 5. Outlook: optimized microdisk geometry for enhanced emitter-photon coupling

The PL mode spectroscopy, and the corresponding analysis presented in Section 3 and 4 shows the promising nature of fiber-taper coupled diamond microdisks. Our analysis indicates that thinner microdisks will be beneficial to reduce the observed multimode nature and relax the phase-matching requirements to the fiber taper. In this section, we explore the potential Purcell enhancement expected for next generation devices with realistic assumptions on fabrication improvements. Utilizing the Purcell effect [38] provides a means to greatly enhance the flux of coherent photons from color centers in diamond by resonant coupling of the ZPL to a single mode in an optical resonator [33]. For an NV center with lifetime limited optical emission linewidth, optimally positioned in the microdisk with the dipole moment aligned perfectly with the optical field, the Purcell factor $C_{ZPL}$ is given by [75,105]:

$$C_{ZPL} = \zeta_{ZPL}\frac{3}{4\pi^2}\frac{Q}{V_{eff}}\left(\frac{\lambda_0}{n}\right)^3, \tag{6}$$

where $\zeta_{ZPL} = 0.03$ is the NV center Debye-Waller factor describing the branching into the ZPL [33,106]. The scaling $C_{ZPL} \propto Q/V$ favours the use of fundamental cavity modes with low $m$, on account of their large $Q$-factor and small $V$ (see Table 3) [17,105].

In Fig. 4(a) and (b), we show laser transmission measurement of diamond microdisks with $[r, t]$=[3.5, 1.0] µm and $[r, t]$=[3.6, 1.0] µm, respectively. Here the low resonance contrast is attributed to poor phase matching with the fiber-taper mode, which is expected for lower order modes of the microdisk: such modes will have larger values of $m$ than their higher-order counterparts of similar wavelength. The doublet nature observed for these modes arises as a

Optics EXPRESS

consequence of back-scattering of light between clockwise (cw) and counterclockwise (ccw) modes due to surface roughness, which lifts their degeneracy and creates orthogonal standing wave modes whose splitting is set by the back-scattering rate and whose quality factors can differ depending on their interaction with imperfection of the microdisk [101,102]. To extract the $Q$-factor, we fit the cavity resonance with a lineshape derived from the coherent sum of two complex Lorentzians [107,108], and find $Q \sim 1 \times 10^5$ at $\lambda \sim 739$ nm for both standing wave modes. These are, to the best of our knowledge, the largest $Q$-factors for SCD resonators at visible wavelength reported to date. Here we focus on modes around $\sim 737$ nm excited by the available laser and resonant with the SiV center [109]. We expect modes at 637 nm, resonant with the NV center ZPL, to have comparable $Q$, depending on the trade-off between mode confinement and surface scattering – both the sensitivity to surface scattering and the mode confinement increases with shorter wavelengths [101,102].

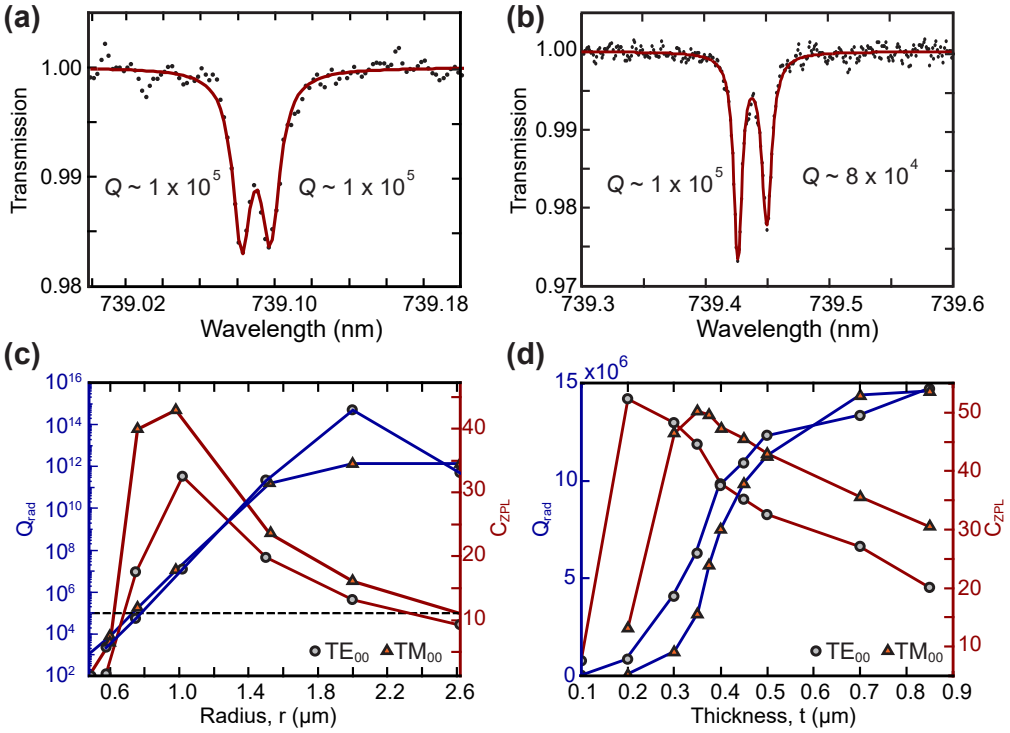


**Fig. 4.** Laser transmission spectroscopy of a diamond microdisk with **(a)** $[r, t]$=[3.5, 1.0] μm and **(b)** $[r, t]$=[3.6, 1.0] μm. A Lorentzian fit to the cavity resonances reveal $Q \sim 1 \times 10^5$ for both devices. This is the largest observed $Q$-factor for a SCD device operating at visible wavelengths. **(c)** Simulation of $Q_{\mathrm{rad}}$ (blue) and $C_{\mathrm{ZPL}}$ (burgundy) for the fundamental TE $(\mathrm{TM})_{00}$ modes as a function of radius $r$ for a microdisk with fixed $t \sim 0.5$ μm. The dashed horizontal line represents $Q_{\mathrm{fab}} = 1 \times 10^5$, as extracted from the fits in (a) and (b). **(d)** Simulated $Q_{\mathrm{rad}}$ (blue) and $C_{\mathrm{ZPL}}$ (burgundy) as a function of thickness for a device with fixed $r \sim 1$ μm. The colored lines in (c) and (d) provide a guide to the eye.

We now turn to discuss a potential route to improve the $Q/V$ ratio for our devices. For a general optical resonator, the total $Q$-factor is given by:

$$\frac{1}{Q_{\mathrm{tot}}} = \frac{1}{Q_{\mathrm{rad}}} + \frac{1}{Q_{\mathrm{mat}}} + \frac{1}{Q_{\mathrm{fab}}}, \tag{7}$$

Optics EXPRESS

where $Q_{rad}$ accounts for radiation loss, $Q_{mat}$ is associated with material absorption and $Q_{fab}$ encompasses surface scattering and absorption resulting from fabrication imperfections [69,102]. Reducing the microdisk dimensions constitutes a method to simultaneously improve the coupling to lower-order fundamental modes and decreasing $V$. Although $Q_{rad}$ is expected to decrease with microdisk $r$ and $t$, in this work, we expect $Q_{fab}$ to be the dominant limitation to $Q_{tot}$. As the relative contribution from fabrication induced imperfections in degrading $Q_{tot}$ increases with smaller disk size, $1 \times 10^5$ (Fig. 4(a) and (b)) provides a realistic upper-limit on $Q_{fab}$ expected with the current state-of-the-art fabrication techniques [69]. Therefore, in the following analysis, we set $Q_{fab} = 10^5$ as the upper limit to $Q_{tot}$ i.e. $Q_{tot}^{-1} = Q_{rad}^{-1} + 10^{-5}$, where we have ignored $Q_{mat}$ on the grounds of the low absorption in diamond.

In Fig. 4(c) and (d), we simulate the behaviour of $Q_{rad}$ as a function of $r$ and $t$, respectively. As expected, we observe an increase in $Q_{rad}$ with increasing $r$ and $t$ (blue lines in Fig. 4(c) and (d)). Furthermore, as indicated by the horizontal dashed line in Fig. 4(c), $Q_{rad}$ only becomes the dominant limitation for $Q_{tot}$ for $r$<0.8 μm – significantly smaller than the range of $r$ for the microdisks studied in this work. This observation supports our assumption that $Q_{fab}$ is the dominant limitation to $Q_{tot}$.

We next estimate the Purcell factor, $C_{ZPL}$, expected for our devices at smaller $r$ and $t$. The burgundy lines in Fig. 4(c) and (d) evaluate the theoretical $C_{ZPL}$ according to Eq. (7) as a function of the microdisk radius and thickness, respectively. Here we have again used $Q_{tot}^{-1} = Q_{rad}^{-1} + 10^{-5}$, thus assuming we can maintain $Q_{fab}$ for the smaller devices. In Fig. 4(c) the thickness is fixed at $t = 0.5\,\mu$m, and the radius is varied, from which we find that $r = 1.0\,\mu$m is optimal for this thickness. In Fig. 4(d) we then vary thickness with $r$ fixed at this value, and find that $C_{ZPL}$ can be further enhanced by reducing $t \sim 400$ nm, where $C_{ZPL} \sim 50$ is predicted. Note that further simultaneous optimization of $t$ and $r$ may result in additional increases to $C_{ZPL}$. At this thickness, the devices will have $\tilde{t} = 1.4\,\lambda$ – comparable to what is achieved with the current devices measured at telecom wavelengths [80].

Select literature values for $C_{ZPL}$, as well as the emitter-independent value $C = C_{ZPL}/\zeta_{ZPL}$, are presented in Table 4. The results presented in Fig. 4(d) demonstrate that, provided fabrication-related losses can be controlled, diamond microdisks have the ability to match the $C_{ZPL}$ achievable with other state-of-the-art on-chip devices, while providing a broader mode spectrum and direct low-loss coupling without integrated fiber couplers [67,89].

**Table 4. Expected Purcell factors for SCD devices calculated from the cavity properties as reported in the selected literature.**

| Ref. | Geometry | Material | $C$ | $C_{ZPL}$ |
|---|---|---|---|---|
| [43] | Microdisk | GaP on diamond | 20 | 0.6 |
| [40] | Photonic crystal cavity | Diamond | 260 | 7.8 |
| [67] | Photonic crystal cavity | Diamond | 1600 | 48 |
| [82] | Photonic crystal cavity | Diamond | 1300 | 39 |
| This Work | Microdisk | Diamond | 1670 | 50 |

## 6. Conclusion

We have performed room temperature optical spectroscopy of single-crystal diamond microdisks using fiber-taper collected PL from an ensemble of NV centers. The relative intensities of resonances in the PL signal compared to those predicted from transmission measurement of mode properties suggest that the PSB emission is filtered not only by the cavity spectrum but also by the mode-dependent coupling between the microdisk and the fiber taper. A comparison between the measured and simulated FSR implies that, for the devices studied here, there is preferential fiber coupling to higher-order radial modes of relatively high $Q$-factor ($10^3 - 10^4$). This preferential

Optics EXPRESS

coupling is likely a consequence of a more favourable phase-matching conditions. The relatively poor coupling to the fiber taper limits the characterization of the highest-$Q$ mode families with fiber collection. However, thinning of the microdisks to $\tilde{t} \sim 1.4\lambda$ should simultaneously improve the phase-matching-limited fiber-taper coupling and reduce the multi-mode nature of the microdisks by freezing out higher-order vertical modes. If the highest measured $Q_{\mathrm{fab}} \sim 1 \times 10^5$ can be achieved in such small devices, diamond microdisks should be able to achieve Purcell factors $C_{\mathrm{ZPL}} \sim 50$, matching those of other state-of-the-art devices while providing broader mode spectrum and alternative integrated coupling options. Observation of NV lifetime reduction and zero phonon line enhancement using these devices will become possible in future through operation at cryogenic temperatures.

**Funding.** Canada Foundation for Innovation; Alberta Innovates; Natural Sciences and Engineering Research Council of Canada.

**Acknowledgments.** This work was supported by funding from the National Sciences and Engineering Research Council of Canada (NSERC), Alberta Innovates – Technology Futures (AITF) and National Research Council Nanotechnology Research Centre NanoInitiative. SF acknowledges support from the Swiss National Science Foundation (Project No. P500PT_206919).

**Disclosures.** The authors declare no conflicts of interest.

**Data availability.** Data underlying the results presented in this paper are not publicly available at this time but may be obtained from the authors upon reasonable request.

## References

1. G. Balasubramanian, P. Neumann, D. Twitchen, *et al.*, "Ultralong spin coherence time in isotopically engineered diamond," Nat. Mater. **8**(5), 383–387 (2009).
2. M. H. Abobeih, J. Cramer, M. A. Bakker, *et al.*, "One-second coherence for a single electron spin coupled to a multi-qubit nuclear-spin environment," Nat. Commun. **9**(1), 2552 (2018).
3. C. E. Bradley, J. Randall, M. H. Abobeih, *et al.*, "A Ten-Qubit Solid-State Spin Register with Quantum Memory up to One Minute," Phys. Rev. X **9**(3), 031045 (2019).
4. P.-J. Stas, Y. Q. Huan, B. Machielse, *et al.*, "Robust multi-qubit quantum network node with integrated error detection," Science **378**(6619), 557–560 (2022).
5. P. Tamarat, N. B. Manson, J. P. Harrison, *et al.*, "Spin-flip and spin-conserving optical transitions of the nitrogen-vacancy centre in diamond," New J. Phys. **10**(4), 045004 (2008).
6. L. Robledo, H. Bernien, T. V. D. Sar, *et al.*, "Spin dynamics in the optical cycle of single nitrogen-vacancy centres in diamond," New J. Phys. **13**(2), 025013 (2011).
7. T. Müller, C. Hepp, B. Pingault, *et al.*, "Optical signatures of silicon-vacancy spins in diamond," Nat. Commun. **5**(1), 3328 (2014).
8. L. J. Rogers, K. D. Jahnke, M. H. Metsch, *et al.*, "All-Optical Initialization, Readout, and Coherent Preparation of Single Silicon-Vacancy Spins in Diamond," Phys. Rev. Lett. **113**(26), 263602 (2014).
9. Y. Chu, M. Markham, D. J. Twitchen, *et al.*, "All-optical control of a single electron spin in diamond," Phys. Rev. A **91**(2), 021801 (2015).
10. J. N. Becker, B. Pingault, D. Groß, *et al.*, "All-Optical Control of the Silicon-Vacancy Spin in Diamond at Millikelvin Temperatures," Phys. Rev. Lett. **120**(5), 053603 (2018).
11. L. Robledo, L. Childress, H. Bernien, *et al.*, "High-fidelity projective read-out of a solid-state spin quantum register," Nature **477**(7366), 574–578 (2011).
12. D. D. Sukachev, A. Sipahigil, C. T. Nguyen, *et al.*, "Silicon-Vacancy Spin Qubit in Diamond: A Quantum Memory Exceeding 10 ms with Single-Shot State Readout," Phys. Rev. Lett. **119**(22), 223602 (2017).
13. D. M. Irber, F. Poggiali, F. Kong, *et al.*, "Robust all-optical single-shot readout of nitrogen-vacancy centers in diamond," Nat. Commun. **12**(1), 532 (2021).
14. S. Johnson, P. R. Dolan, and J. M. Smith, "Diamond photonics for distributed quantum networks," Prog. Quantum Electron. **55**, 129–165 (2017).
15. D. D. Awschalom, R. Hanson, J. Wrachtrup, *et al.*, "Quantum technologies with optically interfaced solid-state spins," Nat. Photonics **12**(9), 516–527 (2018).
16. M. Ruf, N. H. Wan, H. Choi, *et al.*, "Quantum networks based on color centers in diamond," J. Appl. Phys. **130**(7), 070901 (2021).
17. P. K. Shandilya, S. Flågan, N. C. Carvalho, *et al.*, "Diamond Integrated Quantum Nanophotonics: Spins, Photons and Phonons," J. Lightwave Technol. **40**(23), 7538–7571 (2022).
18. M. W. Doherty, N. B. Manson, P. Delaney, *et al.*, "The nitrogen-vacancy colour centre in diamond," Phys. Rep. **528**(1), 1–45 (2013).
19. M. V. G. Dutt, L. Childress, L. Jiang, *et al.*, "Quantum Register Based on Individual Electronic and Nuclear Spin Qubits in Diamond," Science **316**(5829), 1312–1316 (2007).

Optics EXPRESS


20. G. D. Fuchs, G. Burkard, P. V. Klimov, *et al.*, "A quantum memory intrinsic to single nitrogen–vacancy centres in diamond," Nat. Phys. **7**(10), 789–793 (2011).
21. C. E. Bradley, S. W. de Bone, P. F. W. Möller, *et al.*, "Robust quantum-network memory based on spin qubits in isotopically engineered diamond," npj Quantum Inf. **8**(1), 122 (2022).
22. M. H. Abobeih, Y. Wang, J. Randall, *et al.*, "Fault-tolerant operation of a logical qubit in a diamond quantum processor," Nature **606**(7916), 884–889 (2022).
23. E. Togan, Y. Chu, A. S. Trifonov, *et al.*, "Quantum entanglement between an optical photon and a solid-state spin qubit," Nature **466**(7307), 730–734 (2010).
24. H. Bernien, B. Hensen, W. Pfaff, *et al.*, "Heralded entanglement between solid-state qubits separated by three metres," Nature **497**(7447), 86–90 (2013).
25. B. Hensen, H. Bernien, A. E. Dréau, *et al.*, "Loophole-free Bell inequality violation using electron spins separated by 1.3 kilometres," Nature **526**(7575), 682–686 (2015).
26. N. Kalb, A. A. Reiserer, P. C. Humphreys, *et al.*, "Entanglement distillation between solid-state quantum network nodes," Science **356**(6341), 928–932 (2017).
27. W. Pfaff, B. J. Hensen, H. Bernien, *et al.*, "Unconditional quantum teleportation between distant solid-state quantum bits," Science **345**(6196), 532–535 (2014).
28. M. Pompili, S. L. N. Hermans, S. Baier, *et al.*, "Realization of a multinode quantum network of remote solid-state qubits," Science **372**(6539), 259–264 (2021).
29. S. L. N. Hermans, M. Pompili, H. K. C. Beukers, *et al.*, "Qubit teleportation between non-neighbouring nodes in a quantum network," Nature **605**(7911), 663–668 (2022).
30. H. J. Kimble, "The quantum internet," Nature **453**(7198), 1023–1030 (2008).
31. S. Wehner, D. Elkouss, and R. Hanson, "Quantum internet: A vision for the road ahead," Science **362**(6412), eaam9288 (2018).
32. P. C. Humphreys, N. Kalb, J. P. J. Morits, *et al.*, "Deterministic delivery of remote entanglement on a quantum network," Nature **558**(7709), 268–273 (2018).
33. D. Riedel, I. Söllner, B. J. Shields, *et al.*, "Deterministic Enhancement of Coherent Photon Generation from a Nitrogen-Vacancy Center in Ultrapure Diamond," Phys. Rev. X **7**(3), 031040 (2017).
34. S. Guha, H. Krovi, C. A. Fuchs, *et al.*, "Rate-loss analysis of an efficient quantum repeater architecture," Phys. Rev. A **92**(2), 022357 (2015).
35. K. J. Vahala, "Optical microcavities," Nature **424**(6950), 839–846 (2003).
36. D. Wang, H. Kelkar, D. Martin-Cano, *et al.*, "Turning a molecule into a coherent two-level quantum system," Nat. Phys. **15**(5), 483–489 (2019).
37. D. Najer, I. Söllner, P. Sekatski, *et al.*, "A gated quantum dot strongly coupled to an optical microcavity," Nature **575**(7784), 622–627 (2019).
38. E. M. Purcell, H. C Torrey, and R. V. Pound, "Resonance Absorption by Nuclear Magnetic Moments in a Solid," Phys. Rev. **69**(1-2), 37–38 (1946).
39. A. Faraon, P. E. Barclay, C. Santori, *et al.*, "Resonant enhancement of the zero-phonon emission from a colour centre in a diamond cavity," Nat. Photonics **5**(5), 301–305 (2011).
40. A. Faraon, C. Santori, Z. Huang, *et al.*, "Coupling of nitrogen-vacancy centers to photonic crystal cavities in monocrystalline diamond," Phys. Rev. Lett. **109**(3), 033604 (2012).
41. M. Ruf, M. Weaver, S. van Dam, *et al.*, "Resonant Excitation and Purcell Enhancement of Coherent Nitrogen-Vacancy Centers Coupled to a Fabry-Perot Microcavity," Phys. Rev. Appl. **15**(2), 024049 (2021).
42. K.-M. C. Fu, C. Santori, P. E. Barclay, *et al.*, "Coupling of nitrogen-vacancy centers in diamond to a GaP waveguide," Appl. Phys. Lett. **93**(23), 234107 (2008).
43. P. E. Barclay, K.-M. C. Fu, C. Santori, *et al.*, "Chip-based microcavities coupled to nitrogen-vacancy centers in single crystal diamond," Appl. Phys. Lett. **95**(19), 191115 (2009).
44. P. E. Barclay, K.-M. C. Fu, C. Santori, *et al.*, "Hybrid Nanocavity Resonant Enhancement of Color Center Emission in Diamond," Phys. Rev. X **1**(1), 011007 (2011).
45. M. Gould, E. R. Schmidgall, S. Dadgostar, *et al.*, "Efficient Extraction of Zero-Phonon-Line Photons from Single Nitrogen-Vacancy Centers in an Integrated GaP-on-Diamond Platform," Phys. Rev. Appl. **6**(1), 011001 (2016).
46. E. R. Schmidgall, S. Chakravarthi, M. Gould, *et al.*, "Frequency Control of Single Quantum Emitters in Integrated Photonic Circuits," Nano Lett. **18**(2), 1175–1179 (2018).
47. K. G. Fehler, L. Antoniuk, N. Lettner, *et al.*, "Hybrid quantum photonics based on artificial atoms placed inside one hole of a photonic crystal cavity," ACS Photonics **8**(9), 2635–2641 (2021).
48. D. Riedel, H. Lee, J. F. Herrmann, *et al.*, "Efficient photonic integration of diamond color centers and thin-film lithium niobate," ACS Photonics, **10**(12) 4236 (2023).
49. R. Albrecht, A. Bommer, C. Deutsch, *et al.*, "Coupling of a Single Nitrogen-Vacancy Center in Diamond to a Fiber-Based Microcavity," Phys. Rev. Lett. **110**(24), 243602 (2013).
50. S. Johnson, P. R. Dolan, T. Grange, *et al.*, "Tunable cavity coupling of the zero phonon line of a nitrogen-vacancy defect in diamond," New J. Phys. **17**(12), 122003 (2015).
51. H. Kaupp, T. Hümmer, M. Mader, *et al.*, "Purcell-enhanced single-photon emission from nitrogen-vacancy centers coupled to a tunable microcavity," Phys. Rev. Appl. **6**(5), 054010 (2016).

Optics EXPRESS


52. J. Benedikter, H. Kaupp, T. Hümmer, *et al.*, "Cavity-Enhanced Single-Photon Source Based on the Silicon-Vacancy Center in Diamond," Phys. Rev. Appl. **7**(2), 024031 (2017).
53. S. Häußler, J. Benedikter, K. Bray, *et al.*, "Diamond photonics platform based on silicon vacancy centers in a single-crystal diamond membrane and a fiber cavity," Phys. Rev. B **99**(16), 165310 (2019).
54. R. Høy Jensen, E. Janitz, Y. Fontana, *et al.*, "Cavity-enhanced photon emission from a single germanium-vacancy center in a diamond membrane," Phys. Rev. Appl. **13**(6), 064016 (2020).
55. G. Bayer, R. Berghaus, S. Sachero, *et al.*, "Optical driving, spin initialization and readout of single SiV- centers in a Fabry-Perot resonator," Commun. Phys. **6**(1), 300 (2023).
56. N. H. Wan, T. J. Lu, K. C. Chen, *et al.*, "Large-scale integration of artificial atoms in hybrid photonic circuits," Nature **583**(7815), 226–231 (2020).
57. S. B. van Dam, M. Walsh, M. J. Degen, *et al.*, "Optical coherence of diamond nitrogen-vacancy centers formed by ion implantation and annealing," Phys. Rev. B **99**(16), 161203 (2019).
58. M. Kasperczyk, J. A. Zuber, J. Kölbl, *et al.*, "Statistically modeling optical linewidths of nitrogen vacancy centers in microstructures," Phys. Rev. B **102**(7), 075312 (2020).
59. S. Chakravarthi, C. Pederson, Z. Kazi, *et al.*, "Impact of surface and laser-induced noise on the spectral stability of implanted nitrogen-vacancy centers in diamond," Phys. Rev. B **104**(8), 085425 (2021).
60. V. Yurgens, J. A. Zuber, S. Flågan, *et al.*, "Low-charge-noise nitrogen-vacancy centers in diamond created using laser writing with a solid-immersion lens," ACS Photonics **8**(6), 1726–1734 (2021).
61. B. McCullian, H. Cheung, H. Chen, *et al.*, "Quantifying the spectral diffusion of N- V centers by symmetry," Phys. Rev. Appl. **18**(6), 064011 (2022).
62. M. J. Burek, Y. Chu, M. S. Z. Liddy, *et al.*, "High quality-factor optical nanocavities in bulk single-crystal diamond," Nat. Commun. **5**(1), 5718 (2014).
63. M. J. Burek, J. D. Cohen, S. M. Meenehan, *et al.*, "Diamond optomechanical crystals," Optica **3**(12), 1404 (2016).
64. P. Appel, E. Neu, M. Ganzhorn, *et al.*, "Fabrication of all diamond scanning probes for nanoscale magnetometry," Rev. Sci. Instrum. **87**(6), 063703 (2016).
65. A. Sipahigil, R. E. Evans, D. D. Sukachev, *et al.*, "An integrated diamond nanophotonics platform for quantum-optical networks," Science **354**(6314), 847–850 (2016).
66. S. Castelletto, L. Rosa, J. Blackledge, *et al.*, "Advances in diamond nanofabrication for ultrasensitive devices," Microsyst. Nanoeng. **3**(1), 17061 (2017).
67. M. J. Burek, C. Meuwly, R. E. Evans, *et al.*, "Fiber-coupled diamond quantum nanophotonic interface," Phys. Rev. Appl. **8**(2), 024026 (2017).
68. M. Challier, S. Sonusen, A. Barfuss, *et al.*, "Advanced fabrication of single-crystal diamond membranes for quantum technologies," Micromachines **9**(4), 148 (2018).
69. M. Mitchell, D. P. Lake, and P. E. Barclay, "Realizing Q > 300 000 in diamond microdisks for optomechanics via etch optimization," APL Photonics **4**(1), 016101 (2019).
70. C. T. Nguyen, D. D. Sukachev, M. K. Bhaskar, *et al.*, "An integrated nanophotonic quantum register based on silicon-vacancy spins in diamond," Phys. Rev. B **100**(16), 165428 (2019).
71. N. Hedrich, D. Rohner, M. Batzer, *et al.*, "Parabolic diamond scanning probes for single-spin magnetic field imaging," Phys. Rev. Appl. **14**(6), 064007 (2020).
72. Y. Duan, K. C. Chen, D. R. Englund, *et al.*, "A vertically-loaded diamond microdisk resonator spin-photon interface," Opt. Express **29**(26), 43082 (2021).
73. M. J. Burek, N. P. De Leon, B. J. Shields, *et al.*, "Free-standing mechanical and photonic nanostructures in single-crystal diamond," Nano Lett. **12**(12), 6084–6089 (2012).
74. E. Janitz, M. Ruf, M. Dimock, *et al.*, "Fabry-Perot microcavity for diamond-based photonics," Phys. Rev. A **92**(4), 043844 (2015).
75. S. Flågan, D. Riedel, A. Javadi, *et al.*, "A diamond-confined open microcavity featuring a high quality-factor and a small mode-volume," J. Appl. Phys. **131**(11), 113102 (2022).
76. S. Flågan, P. Maletinsky, R. J. Warburton, *et al.*, "Microcavity platform for widely tunable optical double resonance," Optica **9**(10), 1197 (2022).
77. M. K. Bhaskar, R. Riedinger, B. Machielse, *et al.*, "Experimental demonstration of memory-enhanced quantum communication," Nature **580**(7801), 60–64 (2020).
78. B. Khanaliloo, H. Jayakumar, A. C. Hryciw, *et al.*, "Single-crystal diamond nanobeam waveguide optomechanics," Phys. Rev. X **5**(4), 041051 (2015).
79. B. Khanaliloo, M. Mitchell, A. C. Hryciw, *et al.*, "High- Q / V monolithic diamond microdisks fabricated with quasi-isotropic etching," Nano Lett. **15**(8), 5131–5136 (2015).
80. M. Mitchell, B. Khanaliloo, D. P. Lake, *et al.*, "Single-crystal diamond low-dissipation cavity optomechanics," Optica **3**(9), 963 (2016).
81. J. Riedrich-Möller, L. Kipfstuhl, C. Hepp, *et al.*, "One- and two-dimensional photonic crystal microcavities in single crystal diamond," Nat. Nanotechnol. **7**(1), 69–74 (2012).
82. S. Mouradian, N. H. Wan, T. Schröder, *et al.*, "Rectangular photonic crystal nanobeam cavities in bulk diamond," Appl. Phys. Lett. **111**(2), 021103 (2017).
83. B. J. M. Hausmann, B. J. Shields, Q. Quan, *et al.*, "Coupling of NV centers to photonic crystal nanobeams in diamond," Nano Lett. **13**(12), 5791–5796 (2013).

Optics EXPRESS


84. T. Jung, J. Görlitz, B. Kambs, *et al.*, "Spin measurements of NV centers coupled to a photonic crystal cavity," APL Photonics **4**(12), 1–13 (2019).
85. D. P. Lake, M. Mitchell, Y. Kamaliddin, *et al.*, "Optomechanically induced transparency and cooling in thermally stable diamond microcavities," ACS Photonics **5**(3), 782–787 (2018).
86. M. Mitchell, D. P. Lake, and P. E. Barclay, "Optomechanically amplified wavelength conversion in diamond microcavities," Optica **6**(7), 832 (2019).
87. D. P. Lake, M. Mitchell, B. C. Sanders, *et al.*, "Two-colour interferometry and switching through optomechanical dark mode excitation," Nat. Commun. **11**(1), 2208 (2020).
88. P. K. Shandilya, D. P. Lake, M. J. Mitchell, *et al.*, "Optomechanical interface between telecom photons and spin quantum memory," Nat. Phys. **17**(12), 1420–1425 (2021).
89. C. P. Michael, M. Borselli, T. J. Johnson, *et al.*, "An optical fiber taper probe for wafer-scale microphotonic device characterization," Opt. Express **15**(8), 4745 (2007).
90. A. Yariv and P. Yeh, *Photonics: Optical electronics in modern communications* (Oxford University Press, 2006), 6th ed.
91. D. Riedel, S. Flågan, P. Maletinsky, *et al.*, "Cavity-enhance Raman scattering for in situ alignment and characterization of solid-state microcavities," Phys. Rev. Appl. **13**(1), 014036 (2020).
92. H. Kaupp, C. Deutsch, H.-C. Chang, *et al.*, "Scaling laws of the cavity enhancement for nitrogen-vacancy centers in diamond," Phys. Rev. A **88**(5), 053812 (2013).
93. P. R. Dolan, S. Adekanye, A. A. P. Trichet, *et al.*, "Robust, tunable, and high purity triggered single photon source at room temperature using a nitrogen-vacancy defect in diamond in an open microcavity," Opt. Express **26**(6), 7056 (2018).
94. S. M. Spillane, T. J. Kippenberg, O. J. Painter, *et al.*, "Ideality in a fiber taper-coupled microresonator system for application to cavity quantum electrodynamics," Phys. Rev. Lett. **91**(4), 043902 (2003).
95. P. E. Barclay, C. Santori, K.-M. Fu, *et al.*, "Coherent interference effects in a nano-assembled diamond NV center cavity-QED system," Opt. Express **17**(10), 8081 (2009).
96. K. Srinivasan, "Semiconductor optical microcavities for chip-based cavity QED citation," Ph.D. thesis, California Institute of Technology (2006).
97. A. Auffèves, J.-M. Gérard, and J.-P. Poizat, "Pure emitter dephasing: A resource for advanced solid-state single-photon sources," Phys. Rev. A **79**(5), 053838 (2009).
98. A. Meldrum, P. Bianucci, and F. Marsiglio, "Modification of ensemble emission rates and luminescence spectra for inhomogeneously broadened distributions of quantum dots coupled to optical microcavities," Opt. Express **18**(10), 10230 (2010).
99. P. E. Barclay, K. Srinivasan, and O. Painter, "Nonlinear response of silicon photonic crystal microresonators excited via an integrated waveguide and fiber taper," Opt. Express **13**(3), 801 (2005).
100. A. F. Oskooi, D. Roundy, M. Ibanescu, *et al.*, "Meep: A flexible free-software package for electromagnetic simulations by the FDTD method," Comput. Phys. Commun. **181**(3), 687–702 (2010).
101. M. Borselli, K. Srinivasan, P. E. Barclay, *et al.*, "Rayleigh scattering, mode coupling, and optical loss in silicon microdisks," Appl. Phys. Lett. **85**(17), 3693–3695 (2004).
102. M. Borselli, T. J. Johnson, and O. Painter, "Beyond the Rayleigh scattering limit in high-Q silicon microdisks: theory and experiment," Opt. Express **13**(5), 1515 (2005).
103. M. Borselli, "High-Q microresonators as lasing elements for silicon photonics," Ph.d. thesis, california institute of technology, California Institute of Technology (2006).
104. J. Petersen, J. Volz, and A. Rauschenbeutel, "Chiral nanophotonic waveguide interface based on spin-orbit interaction of light," Science **346**(6205), 67–71 (2014).
105. E. Janitz, M. K. Bhaskar, and L. Childress, "Cavity quantum electrodynamics with color centers in diamond," Optica **7**(10), 1232 (2020).
106. C. Santori, P. E. Barclay, K.-M. C. Fu, *et al.*, "Nanophotonics for quantum optics using nitrogen-vacancy centers in diamond," Nanotechnology **21**(27), 274008 (2010).
107. D. S. Weiss, V. Sandoghdar, J. Hare, *et al.*, "Splitting of high-Q Mie modes induced by light backscattering in silica microspheres," Opt. Lett. **20**(18), 1835 (1995).
108. T. J. Kippenberg, S. M. Spillane, and K. J. Vahala, "Modal coupling in traveling-wave resonators," Opt. Lett. **27**(19), 1669 (2002).
109. C. Hepp, T. Müller, V. Waselowski, *et al.*, "Electronic structure of the silicon vacancy color center in diamond," Phys. Rev. Lett. **112**(3), 036405 (2014).